Free Surface Effects on the Near-Inertial Ocean Current Response to a Hurricane: A Revisit

LYNN K. SHAY

Division of Meteorology and Physical Oceanography, Rosenstiel School of Marine and Atmospheric Science, University of Miami, Miami, Florida

SIMON W. CHANG

Marine Meteorology Division, Naval Research Laboratory, Monterey, California

(Manuscript received 16 December 1994, in final form 8 April 1996)

ABSTRACT

Free surface effects induced by an idealized hurricane based on observed air–sea variables in Hurricane Frederic are revisited to examine the barotropic and baroclinic response. Over five inertial periods comparisons between a one-layer and a 17-level model indicate a difference of 6–8 cm s^{-1} in the depth-averaged current and sea level oscillations of 4–5 cm. In a one-layer simulation, the surface slope geostrophically balances the depth-averaged current, whereas the 17-level model simulations indicate a near-inertially oscillating current of 7–8 cm s^{-1} found by removing the depth-averaged flow from the geostrophic currents induced by the surface slope. Surface undulations are driven by the depth-averaged nonlinear terms in the density equation, that is, $[u\rho_x]$, $[v\rho_y]$, and $[w\rho_z]$.

Based on fits of the 17 levels of demodulated horizontal velocities at $1.03f$ (f the Coriolis parameter) to the eigenfunctions, maximum amplitudes of the barotropic and first baroclinic modes are 7 and 58 cm s^{-1}, respectively. The barotropic mode amplitude is consistent with the current found by removing the depth-averaged flow from the geostrophic current that contributes 2%–3% to the energy in the near-inertial wave pass band. Vertical velocity eigenfunctions at the surface indicate that the barotropic mode is at least 50 to 80 times larger than the baroclinic mode. Surface displacements by the barotropic mode have amplitudes of ± 4 cm, explaining 90% to 95% of the height variations. The first baroclinic mode contributes about 0.2–0.4 cm to the free surface displacements. The weak barotropic near-inertial current provides a physical mechanism for the eventual breakup of the sea surface depression induced by the hurricane's wind stress and surface Ekman divergence.

1. Introduction

The oceanic response to the passage of a hurricane has been characterized as a *predominately* baroclinic phenomenon associated with the isopycnal displacements in the thermocline and the excitation of near-inertial oscillations in a spreading three-dimensional pattern. A secondary component is the barotropic response associated with the sea surface depression of 20–30 cm in geostrophic balance with a cyclonically rotating current field (Geisler 1970). Based on heuristic scaling arguments involving the external Froude number, defined as the ratio of the translation speed and the phase speed of the barotropic mode (e.g., Ginis and Sutyrin 1995), theoretical studies have ruled out the existence of barotropic near-inertial oscillations excited by a tropical cyclone passage. This scaling renders the governing equations to be elliptical with nonoscillatory solutions, leading to the assumption of nondivergent flows in the barotropic response. However, recent observations acquired during and subsequent to tropical cyclone passage (e.g., Shay and Elsberry 1987; Hearn and Holloway 1990) indicate that strong baroclinic and weak barotropic[1] currents are excited in the near-inertial wave band. While the geostrophic balance of the sea surface depression and the cyclonically rotating current pattern has been accepted as part of the barotropic response, this weak barotropic oscillation has been deemed unimportant to the near-inertial response and the associated surface dynamics.

Shay et al. (1990, hereafter referred to as SCE) resolved an undulating free surface in the wake of a trop-

Corresponding author address: Dr. Lynn K. Shay, MPO/RSMAS, University of Miami, 4600 Rickenbacker Causeway, Miami, FL 33149-1098.
E-mail: nick@wampee.rsmas.miami.edu

[1] Barotropic mode refers to a depth-independent oscillation in the inertial frequency pass band with a dispersion relation that is similar to the Poincaré wave mode or formally a long wave with rotation $\sigma^2 = f^2 + c_0^2 K_0^2$, where $c_0 = \sqrt{gD}$ and K_0 is the horizontal wave number.

ical cyclone driving a weak, barotropic near-inertial current of 10 cm s^{-1} found in observations acquired during the passage of Hurricane Frederic in the Gulf of Mexico and simulations from a 17-level primitive equation free surface model (Chang 1985). This study was motivated by ocean current and temperature oscillations through the thermocline and into the bottom layers observed with a series of moored current meter arrays in Hurricane Frederic (Shay and Elsberry 1987). The immediate pulse and the excitation of near-inertial oscillations throughout the water column to 457 m (Fig. 1) could not be explained by the dispersion of surface-intensified baroclinic modes (Hopkins 1982) or decomposing the velocity into the bottom slope modes (Lai and Sanford 1986). Based on simulations from analytical and numerical models, this rapid penetration of energy (even to depths of 1000 m) was attributed to the sea surface depression (*barotropic* trough) forced by the wind stress and depth-averaged mass divergence.

Since the oceanic response represents a geostrophic adjustment problem, Rossby (1938) showed that weak barotropic near-inertial oscillations are required for the dispersion of energy from the sea surface depression after removal of the atmospheric forcing. Of the total momentum input by a translating wind stress, approximately 7% of the energy excites barotropic near-inertial oscillations. Similarly, Veronis (1956) estimated about 5% of the momentum from a translating wind field drives barotropic oscillations. These oscillations have periods slightly shorter than the local inertial period (Cahn 1945) causing $\sigma/f > 1$, which occurs for wind-forced near-inertial motions.

The differences between the near-inertial baroclinic and barotropic modes of the evolving three-dimensional velocity structure, as well as their contributions to the surface displacements, are described here. Based upon the vertical structure equation for near-inertial motions subjected to free surface boundary conditions, this approach provides consistency between simulations and the observations allowing for the excitation of currents and temperatures throughout the vertical. Observations are given in section 2 including normal mode eigenfunctions for the barotropic and first few baroclinic modes subjected to both free surface and rigid-lid boundary conditions. Simulations from a one-layer and a 17-level model are described in section 3 within the context of the depth-averaged flow, the geostrophically balanced current, and the sea surface depression. The nonlinear interaction terms are estimated from the depth-averaged momentum and mass equations. In section 4, vertical velocity fields from 18 levels (including the free surface) and the horizontal velocities are fit to the barotropic and first few baroclinic modes. The barotropic and baroclinic modes are evaluated at the sea surface to assess the dominant terms contributing to the free surface displacements. Estimates of the contributions from the barotropic and baroclinic modes to the kinematics and energetics are given with concluding remarks in section 5.

2. Observations

a. Air–sea variables

The ratios governing the barotropic response are the external Froude number (ratio of the translation speed to the phase speed U_h/c_0) and the nondimensional forcing scale (the ratio of the atmospheric forcing scale to the deformation radius of the barotropic mode α_0). The external Froude number is usually small, thereby justifying the neglect of the second-order terms (5%–10%) involving the sea surface evolution in the governing equations. These second-order terms are necessary to balance the fields in the geostrophic adjustment process (Rossby 1938; Cahn 1945). The nondimensional forcing scale depends on the scale of the applied wind field of the tropical cyclone, not just the $2R_{\max}$ (where $R_{\max}$ is the radius of maximum winds) for the positive vorticity curl in baroclinic treatments. For broader and more complex structured storms, cyclonically rotating winds of 10 m s^{-1} may extend 8–10 $R_{\max}$ as observed in Hurricane Frederic (Powell 1982), thereby increasing the forcing scale from $O(0.1)$ to $O(0.5)$ or more. The implication here is that the barotropic response may be driven by the larger-scale wind field. The wavelength (Λ) of the total response is the product of the storm translation speed (U_h) and the inertial period (IP), where Λ is taken to be 580 km for Frederic.

b. Modal structure

In a stratified fluid (see Fig. 7 of SCE), barotropic and baroclinic modes of oscillation are allowed as indicated by the equation for the vertical structure of near-inertial motions for $\sigma^2 \ll N(z)^2$,

$$\frac{d^2\phi_n}{dz^2} + \frac{N^2(z)\phi_n}{c_n^2} = 0, \tag{1}$$

where ϕ_n is the nth eigenfunction of the vertical velocity, $c_n = (\sigma^2 - f^2)^{1/2}/K_n$ is the phase speed of the nth mode ($K_n^2 = k_n^2 + l_n^2$ is the total horizontal wavenumber), σ is the wave frequency, and $N(z)$ is the buoyancy frequency derived from the vertical density gradient. The free surface boundary condition at $z = \eta$ requires pressure to be continuous across the air–sea interface,

$$\frac{d\phi_n}{dz} + \frac{gK_n^2}{\sigma^2 - f^2}\phi_n = 0, \tag{2}$$

and the kinematic bottom boundary condition is $\phi_n = 0$ at $z = -D$.

In a constant N regime, details about the free surface effects on the baroclinic modes are found in the resulting transcendental equation obtained from (2),

$$\tan(mD) = \frac{N^2}{(mD)(g/D)}, \tag{3}$$

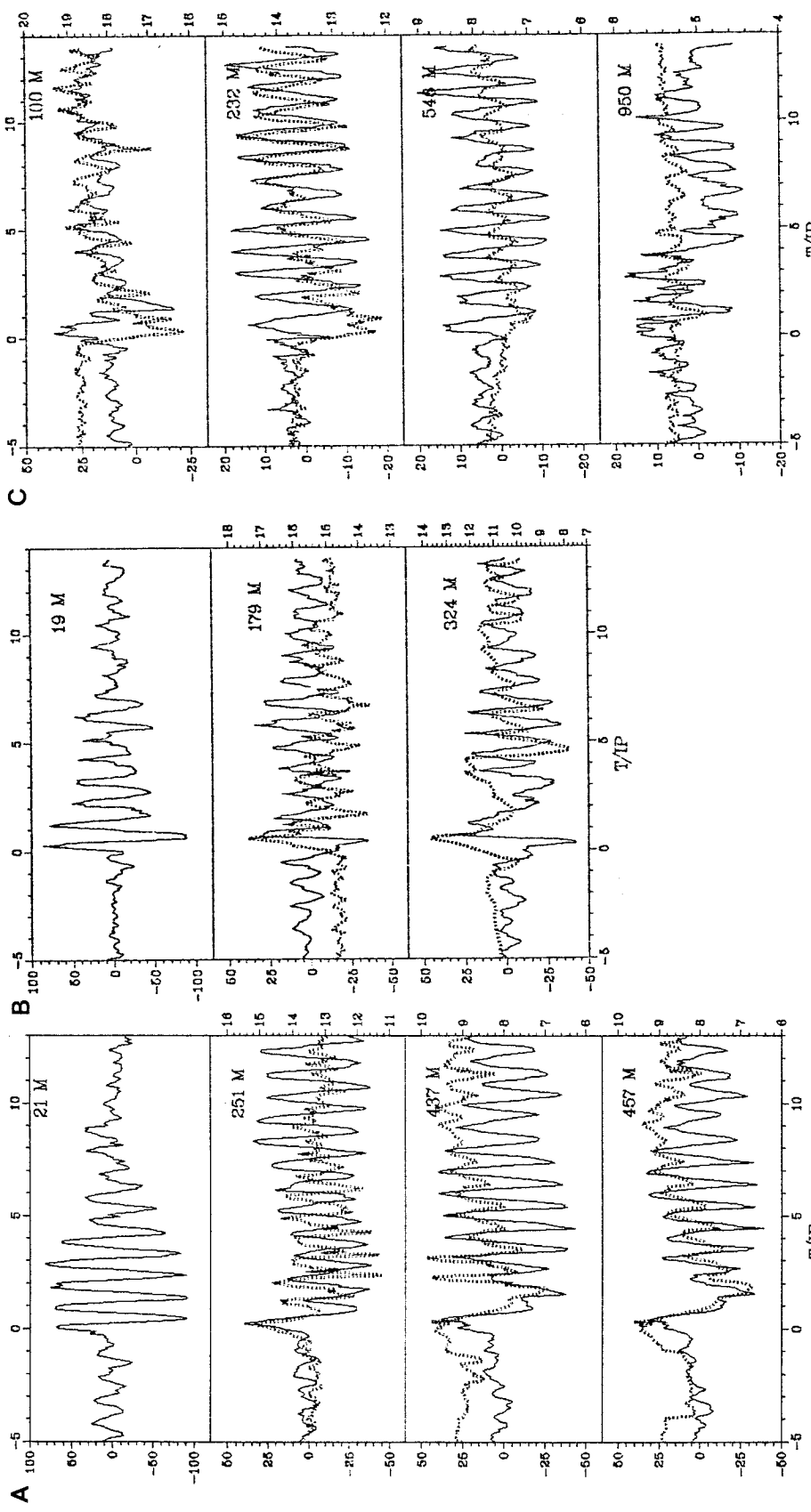

FIG. 1. Alongtrack velocity (cm s^{-1})(solid) and temperature (° C) (dotted) from (a) CMA3, (b) CMA2, and (c) OTEC at depths located in upper right side for each time series normalized by the inertial period relative to the point of closest approach (t = 0). Taut-wire subsurface mooring located approximately 3–5 R_{max} from the point of closest approach of Hurricane Frederic at 2100 UTC 12 Sep 1979 (t = 0) (from Shay and Elsberry 1987).

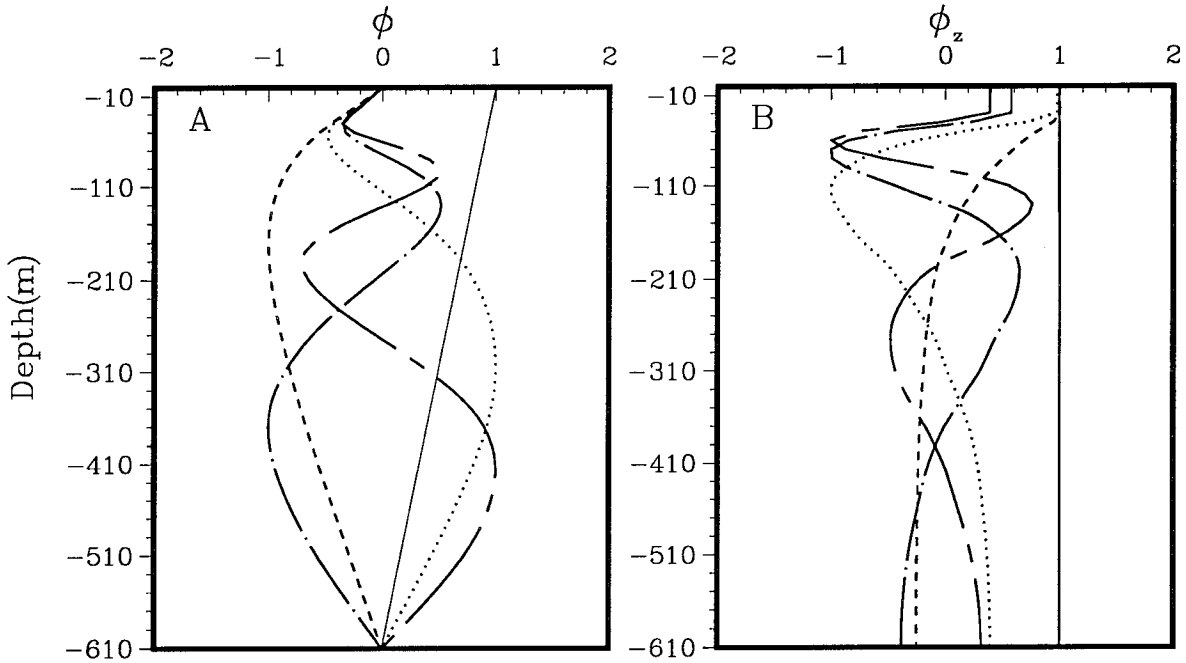

FIG. 2. Normal modes for the (a) vertical velocity (ϕ_n) and (b) horizontal velocity ($d\phi_n/dz$) for the barotropic mode (n = 0: solid), baroclinic mode 1 (dashed), baroclinic mode 2 (dotted), baroclinic mode 3 (chain-dotted), and baroclinic mode 4 (chain-dashed) in an ocean 610 m deep.

where the vertical wavenumber is $m_n^2 \equiv K_n^2/\lambda^2$ and the slope of the wave characteristic is

$$\lambda \equiv \frac{(\sigma^2 - f^2)^{1/2}}{N}.$$

Since

$$\frac{N^2}{(mD)g/D} \approx \frac{10^{-7}}{mD},$$

solutions of (3) will be near the zeros of $\tan(m_nD)$, that is, for $m_nD = \pi, 2\pi, \cdots$(see Fig. 15.2 in Leblond and Mysak 1978). For the barotropic mode (n = 0), $\tan(m_0D) \approx m_0D$; thus

$$m_o = \frac{K_o}{\lambda} = \frac{N}{\sqrt{gD}},$$

or

$$K_o = \frac{(\sigma^2 - f^2)^{1/2}}{\sqrt{gD}}.$$

For the nth baroclinic mode, $m_n = D^{-1}(n\pi + \epsilon_n)$ for $n = 1, 2, \cdots$,where ϵ_n is a correction term such that $D\epsilon_n \ll \pi$, $n \geq 1$, which for the baroclinic modes simplifies to

$$D\epsilon_h \approx \frac{N^2}{n\pi(g/D)}, \qquad n \geq 1.$$

The governing expression for the baroclinic structure is then given by

$$m_n = \frac{n\pi}{D}\left\{1 + \left\{\frac{N^2}{(n\pi)^2 g/D}\right\}\right\}.$$

The second term is $10^{-8}/n^2$; thus, $m_n \approx n\pi/D$ for $n \geq 1$, which is determined from solving (1) subject to a rigid lid. The significance of this expression is that to $O(10^{-7})$, the vertical structure associated with baroclinic near-inertial wave modes is unaffected by the free surface boundary condition.

For a variable N regime, vertical and horizontal velocity eigenfunctions ($u_n = d\phi_n/dz$) for the barotropic and first four baroclinic modes (Fig. 2) were determined for the free surface boundary condition based on an N^2 profile in the Gulf of Mexico (Starr and Maul 1978). The kinematic boundary condition is $w = d\eta/dt$, representing an oscillatory, nonzero vertical velocity at the sea surface associated with the barotropic mode. By contrast, the imposition of a rigid lid ($\phi_n = 0$ at $z = \eta$) eliminates the barotropic mode. The mode-one eigenfunction for the vertical velocity is maximum in the thermocline (200 m), and the maximum vertical velocity of the barotropic mode occurs at the surface, implying that the barotropic and first baroclinic modes are coupled through pressure compensation. That is, the upwelling (downwelling) zone in the thermocline associated with baroclinic processes will be in areas of downward (upward) vertical velocity at the sea surface due to barotropic processes (SCE). In a stratified fluid, modal energies are distributed over the water column as indicated by the observations shown in Fig. 1 and are not confined to the upper layer.

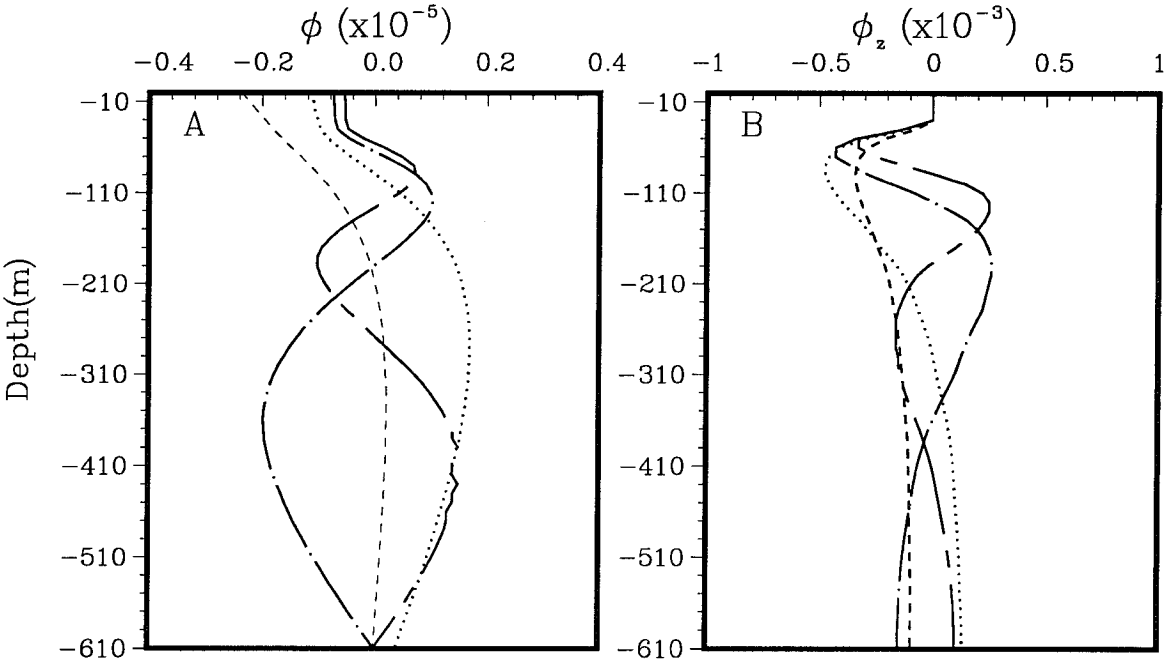

FIG. 3. Differences in the baroclinic modes by solving the vertical structure equation (3) with an imposed rigid lid and free surface boundary conditions for the (a) vertical velocity ($\phi_n \times 10^{-5}$) and (b) horizontal velocity ($d\phi_n/dz \times 10^{-3}$) for the baroclinic mode 1 (dashed), baroclinic mode 2 (dotted), baroclinic mode 3 (chain-dotted), and baroclinic mode 4 (chain-dashed) in an ocean 610 m deep.

The sea surface differences between the baroclinic modes for the vertical velocity eigenfunctions normalized to maximum magnitudes of unity estimated for the rigid-lid and free surface boundary condition are 10^{-6} (Fig. 3). This result implies that the baroclinic modes are insignificantly affected by the inclusion of the free surface condition as shown in (3) above for a constant N regime, which is the reason the rigid-lid approximation yields reasonable numerical results of the ocean's baroclinic response (Price 1983; Greatbatch 1983; Gill 1984).

3. Free surface effects

a. One-layer simulations

The 17-level primitive equation model on an f plane with a free surface (Chang 1985) is collapsed into a one-layer model and forced with a hurricane-like Rankine vortex and air–sea variables that resemble Hurricane Frederic. The details of the model integration and the forcing are described in SCE. The free surface is depressed by about 20 cm elongated along the track as in Fig. 4, which agrees with what was found from the 17-level model in SCE. Oscillatory motion is absent in these sea surface displacements, and the depth-averaged current field rotates cyclonically around the depression with a maximum of about 19 cm s^{-1} (Figs. 4b,c). The circulation pattern resembles an elongated racetrack in geostrophic balance with the gradients in the sea surface depression (Geisler 1970). However, the simulated sea surface depression does not decay after 5–6 Λ, suggesting that it remains long after passage.

b. Seventeen-level model simulations

The 17-1evel primitive equation model with a free surface was originally described in Chang (1985) including the depth-integrated equations with both steady-state and time-dependent terms. To assess the components of the time-dependent free surface deflections, the depth-averaged flow ([ ]) is decomposed into the along-track component

$$[u] = -\frac{g}{f}\frac{\partial \eta}{\partial y} + u_i \tag{4}$$

and the cross-track component

$$[v] = \frac{g}{f}\frac{\partial \eta}{\partial x} + v_i, \tag{5}$$

where the first terms are the geostrophically balanced currents associated with the trough and the second terms represent oscillatory current components. The sea surface height field (η) contributes to the depth-averaged pressure field, and to within an uncertainty of 5%, computing the $\partial\eta/\partial x$ and $\partial\eta/\partial$y in (4) and (5) implies that the horizontal velocities are driven by these depth-averaged pressure gradients. Pedlosky (1979) shows that for $\sigma/f > 1$, oscillatory currents induced by a time-dependent, free surface oscillation will be directed toward the pressure gradient and rotate clockwise. This

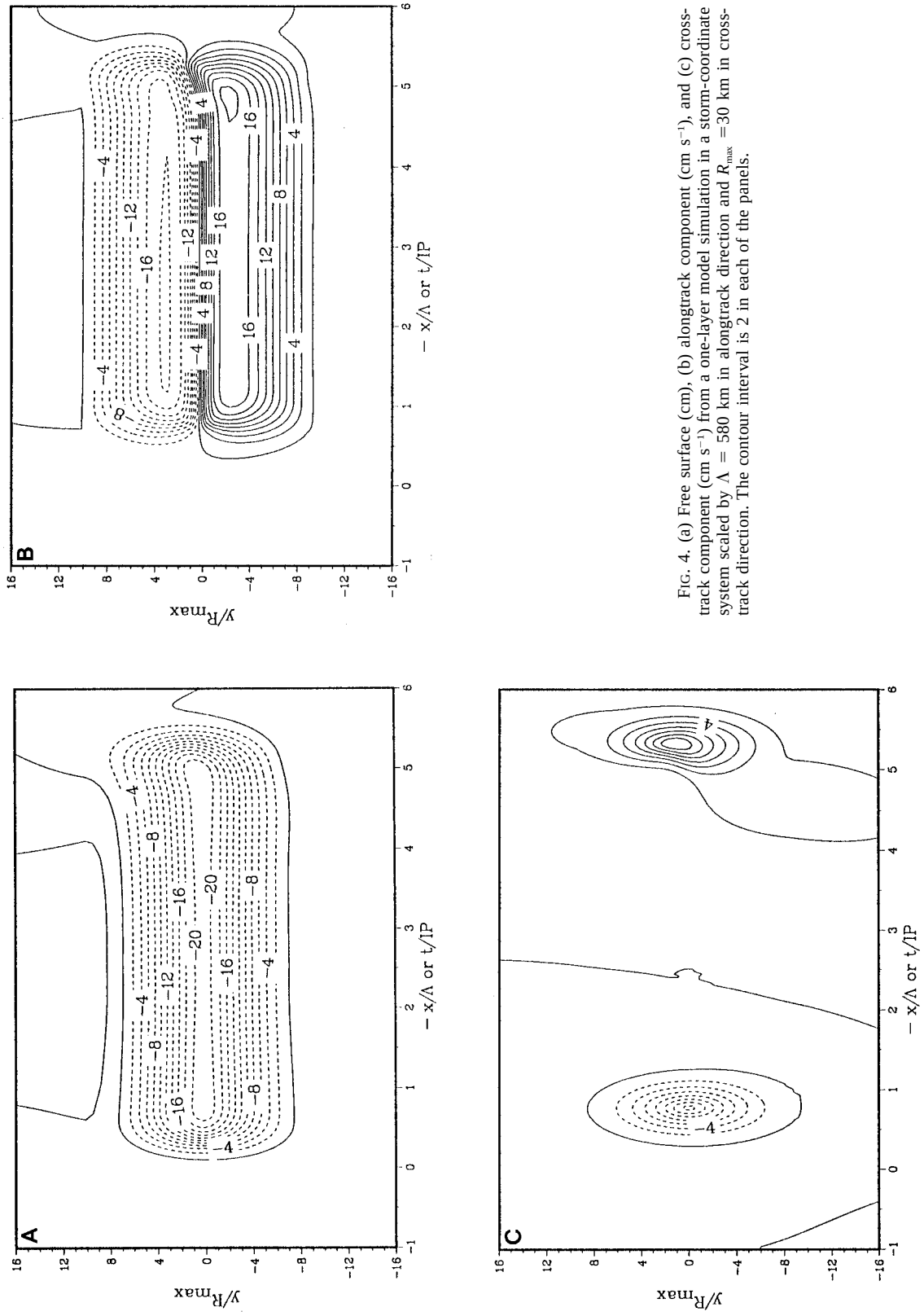

FIG. 4. (a) Free surface (cm), (b) alongtrack component (cm s^{-1}), and (c) cross-track component (cm s^{-1}) from a one-layer model simulation in a storm-coordinate system scaled by Λ = 580 km in alongtrack direction and R_{max} =30 km in cross-track direction. The contour interval is 2 in each of the panels.

is the mechanism that provides for the eventual breakup and decay of the depression (Rossby 1938; Cahn 1945), whereas on a β-plane planetary Rossby waves may play a role in the relaxation of the depression (Geisler 1970).

The variations in the sea surface elevation range from ± 4–5 cm in the sea surface depression (Fig. 5). The maximum depression is 20 cm from the undisturbed level as in the one-layer simulation beginning at 0.5Λ behind the storm. There is also a larger-scale wave of O(1000 km) in the sea surface height field that disperses from the disturbed area as found in SCE, which is one of the components described by Ginis and Sutyrin (1995). As shown in Fig. 5b, the depth-averaged velocities indicate maximum currents of 12 cm s^{-1} rotating cyclonically around the depression, resulting in a net difference of about 7 cm s^{-1} for the same forcing distribution used in the one-layer simulations where the maximum current is 19 cm s^{-1} (Fig. 4). The v component has a small divergent component that contributes to an undulating depth-integrated current over the inertial cycle. Based upon scale analysis, the depth-averaged velocities from the one-layer and 17-level models should be identical for the same forcing distribution and air–sea variables, unless there are depth-independent oscillatory currents embedded within the trough associated with an oscillating sea surface.

Based on the current field derived from the free surface gradients (Fig. 6), on the right (left) side of the storm track ($y = 0$) maximum alongtrack components are 18–20 cm s^{-1} in the direction of (and opposite to) the storm movement. The time-dependent velocity perturbations between $y = \pm 6R_{max}$, with maximum speeds of about 7 cm s^{-1}, oscillate at similar inertial wavelengths (Λ) of 580 km. After the initial spinup, cross-track and alongtrack components oscillate with amplitudes of 2 and 7 cm s^{-1}, respectively. The depth-averaged pressure gradient causes a compensating inertially rotating current. This oscillating flow field is isolated by subtracting the depth-averaged velocities (Fig. 5) from the geostrophic currents (Fig. 6) and superposing them on the residual free surface undulations computed by differencing one-layer and 17-level free surface height fields (Fig. 7). The salient feature here is the net divergence and convergence cycle of the cross-track velocity of about 7 cm s^{-1} over near-inertial wavelengths in the direction of the pressure gradient starting at $x =$ 0.5 to 1 Λ (Pedlosky 1979). This pattern is remarkably similar to that found in SCE (e.g., Fig. 4) determined by convolving the sea surface elevation pattern with a Green's function. However, the current speeds of 7–8 cm s^{-1} are smaller than previous estimates of 10–11 cm s^{-1}, with periods slightly shorter than the inertial period ($\sigma/f > 1$) (Cahn 1945). In an ocean 465 m deep (similar to the ocean depth where CMA3 was deployed in Fig. 1), the equivalent barotropic current, estimated from $u_{610}D_{610} = u_{465}D_{465}$, is 9–10 cm s^{-1}, which agrees with the observed depth-averaged oscillation shown in Fig. 6 of SCE. Since there is an inertial oscillation with a wavelength Λ, the depth-independent velocity component should be found in the demodulated current signals.

c. Vertical velocity

The vertical velocity at the sea surface is in phase with the vertical velocity at 5 m determined by vertically integrating the horizontal divergence of the currents starting at $z = -D$ (Fig. 8). Maximum vertical velocities estimated from η_t are 10^{-3} cm s^{-1} compared to 8×10^{-4} cm s^{-1} at 5 m or a difference of 2×10^{-4} cm s^{-1}. Over the next half of the inertial cycle, these values are 4×10^{-4} cm s^{-1} at 5 m and the surface. Vertical velocity oscillations of 2×10^{-4} cm s^{-1} are associated with the surface displacements except at $x = 5.5\Lambda$. For the free surface distribution, the vertical velocity at the sea surface is directed downward with maximum values of about 8×10^{-4} cm s^{-1}, occurring immediately to the right of the storm track. By contrast, vertical velocities in the thermocline are upward at the corresponding locations of the downward vertical velocities at the sea surface, which is consistent with a phase relationship due to the pressure compensation tendency.

d. Nonlinear terms

To isolate the mechanism that induces the free surface oscillations, the nonlinear interaction terms from the momentum and mass (density) balance are depth integrated (Fig. 9). Since the nonlinear momentum terms are products of $\cos(\sigma t)$ and $\sin(\sigma t)$ trigonometric functions, the result is that these terms excite oscillations with periods of one-half the inertial period or $\frac{1}{2}\sin(2\sigma t)$ (Fig. 9a). These nonlinear interaction terms involving both the baroclinic and barotropic components have minimal influence on the inertial oscillations of the free surface but may be a second-order correction term to the displacements. The depth-averaged products of the nonlinear terms from the prognostic equation for mass or density ($[u\rho_x]$, $[v\rho_y]$, $[w\rho_z]$) indicates a sinusoidal variation in all three terms over an inertial period (Fig. 9b). The dominant component is $[v\rho_y]$, which is a factor of 2 larger than the $[w\rho_z]$ term, and three to four times larger than the $[u\rho_x]$ term. The addition of these terms represent the baroclinic and barotropic interactions between the velocities and the density gradients, or the depth-averaged mass divergence (Chang 1985). The oscillatory depth-averaged density and pressure field induced by this mass divergence requires a compensating current since the depth-averaged flow is not fully geostrophically balanced according to (4) and (5). In the one-layer model simulation above, there are no horizontal density gradients and an absence of these surface oscillations.

The terms in the prognostic equation for the free surface (η) provide insight into the balance of forces:

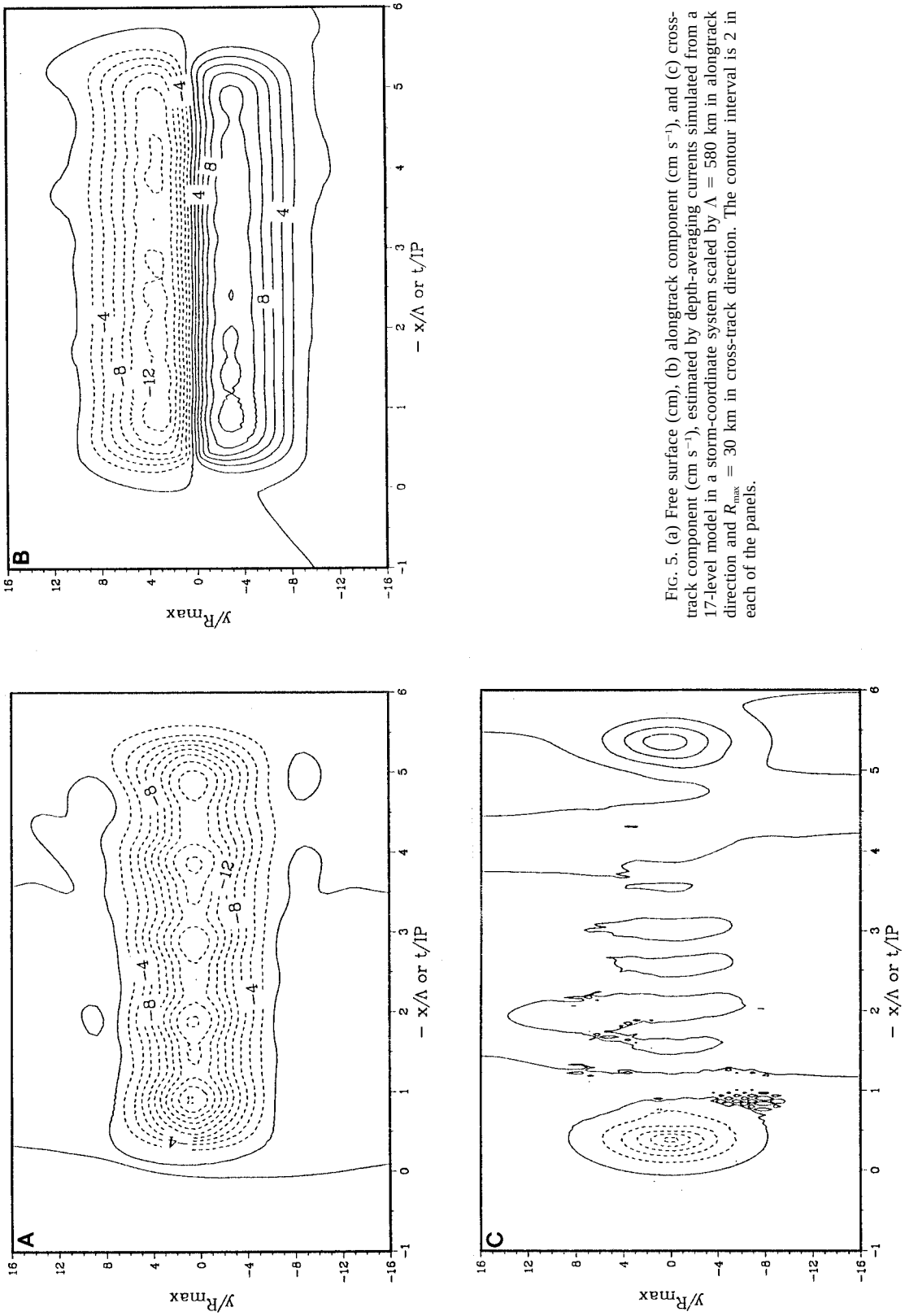

FIG. 5. (a) Free surface (cm), (b) alongtrack component (cm s^{-1}), and (c) cross-track component (cm s^{-1}), estimated by depth-averaging currents simulated from a 17-level model in a storm-coordinate system scaled by $\Lambda = 580$ km in alongtrack direction and $R_{max} = 30$ km in cross-track direction. The contour interval is 2 in each of the panels.

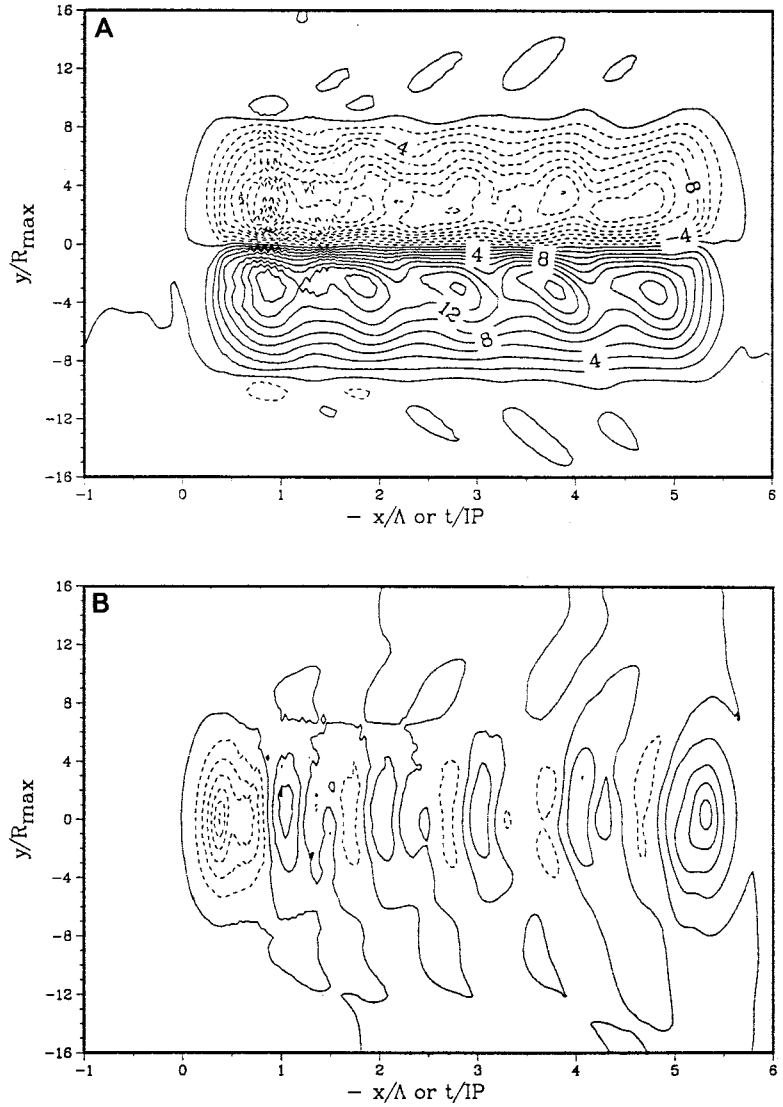

FIG. 6. (a) Alongtrack and (b) cross-track geostrophic current components (cm s^{-1}) estimated from the free surface gradients shown in Fig. 5a. The solid (dashed) contours represent positive (negative) values at an interval of 2 cm s^{-1}. The axes are as in Fig. 5.

$$\frac{\partial \eta}{\partial t} = \underbrace{-D\frac{\partial [u]}{\partial x} - D\frac{\partial [v]}{\partial y}}_{1} \quad \underbrace{-\frac{\partial u_s \eta}{\partial x} - \frac{\partial v_s \eta}{\partial x}}_{2}, \qquad (6)$$

where the vertical velocity at the bottom is assumed to be zero ($w = 0$ at $z = -D$), $[u]$ and $[v]$ represent the depth-averaged current, and u_s and v_s are the surface velocities (Chang 1985). These surface velocities contain both barotropic and baroclinic contributions.

In the direct forcing region, the first (horizontal divergence) term is a maximum of 8×10^{-4} cm s^{-1} and is balanced by the vertical velocity with a slightly smaller value than the relative maximum in η_t of 10^{-3} cm s^{-1} (Fig. 10). The second term (10^{-5} cm s^{-1}) represents a surface transport term that is more than an order of magnitude less than the first term, implying that the balance is between the η_t and the first term in (6). The addition of η_t with this first term indicates a cell in the vicinity of the storm center and a less energetic cell one wavelength in the wake (not shown). The surface transport terms are considerably less than the other terms; however, this oscillatory pattern may modulate surface displacements over the baroclinic decay timescales of $1/\sqrt{x'}(x' = x\lambda_1^{-1}$, where λ_1 is the deformation radius of the first baroclinic mode), following from the asymptotic expansion of J_o (Geisler 1970). According to scaling arguments, the time-dependent sea surface deformations are not directly balanced by the surface transport terms to $O(10^{-4})$ here.

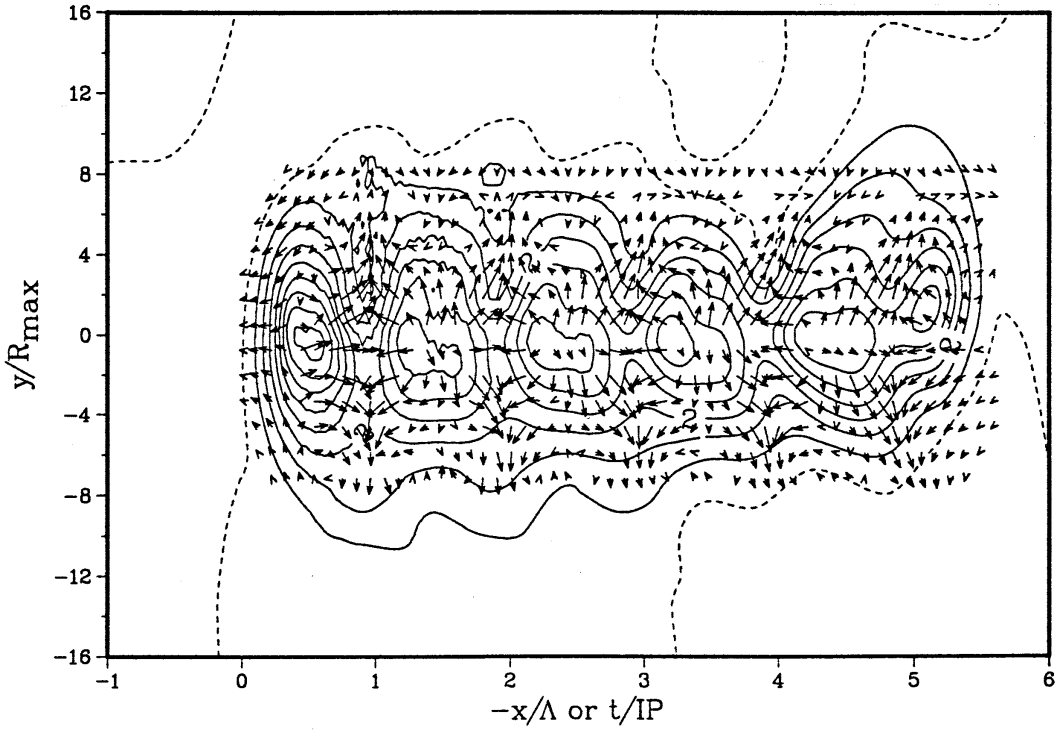

FIG. 7. Current vectors (cm s^{-1}) estimated from subtracting the depth-averaged velocity in Fig. 5 and those calculated from the sea surface gradients in Fig. 6 superposed on contours of sea surface undulations (cm) found by removing the steady-state signal (Fig. 4a to Fig. 5a) from the combined steady-state and transient signals to isolate the transient signals. Notice the oscillatory nature of this current and sea surface fields over the inertial cycle with a speed maximum of 7 cm s^{-1}. The axes are scaled as in Fig. 5, and the contour interval is 1 cm.

4. Near-inertial analysis

a. Frequency

Since sea surface displacements are induced through the depth-averaged mass divergence, the question arises concerning the existence of the oscillatory velocity structure for both the barotropic and baroclinic modes in the directly forced and evolving wake of the storm. And, after the sea surface is displaced, do these velocities behave as linear, weakly nonlinear, or nonlinear oscillations? To examine this question for both the horizontal and vertical velocities, a near-inertial analysis is performed using the simulations projected onto the normal modes (Fig. 2).

The horizontal velocities from the 17-level model are fit to a series of trial frequencies (0.8–1.2 f) to determine the frequency of the oscillations over five IP segments (Mayer et al. 1981). The carrier frequency is defined as the frequency that minimizes the residual signal covariance of the complex-rotating velocity vector. The vertical distribution of the frequencies normalized to f indicates a blue shift occurring between 1% and 5% above f at 5 and 135 m, respectively. This approach accounts for 80% of the observed variance in the mixed layer and thermocline. In the thermocline, carrier frequencies of 1.06–1.07 f are found, whereas at depth the carrier frequencies shift back toward f. These frequency shifts from 1.06f to 1.07f are above the level of uncertainty of 0.02f in the approach (Shay and Elsberry 1987). A frequency of 1.03f will be used here for the 17-levels of simulated velocities as prescribed in the solution of the vertical structure equation (1)–(2).

b. Vertical structure analysis

Demodulated horizontal velocities at 1.03f are combined to form the clockwise-rotating amplitudes and phases associated with the near-inertial response. Maximum anticyclonically rotating amplitudes of about 90–100 cm s^{-1} occur in the mixed layer, while the maximum component is 40–60 cm s^{-1} in the thermocline (70–90 m) (see Fig. 14 in SCE). Between 90 and 175 m, there is a phase reversal of the anticyclonically rotating component, which is consistent with the dominant first baroclinic mode response. Maximum anticyclonically rotating amplitudes are 15–20 cm s^{-1} elongated in the alongtrack direction with a relatively slow decay scale compared to that in the mixed layer.

The real part of the demodulated signals for the horizontal velocity components ($u + iv$) at 15 levels are fit to the modal eigenfunctions from Fig. 2 based upon singular value decomposition (Press et al. 1989). This method has the advantage of minimizing leakage between the various modes in that energy is conserved in

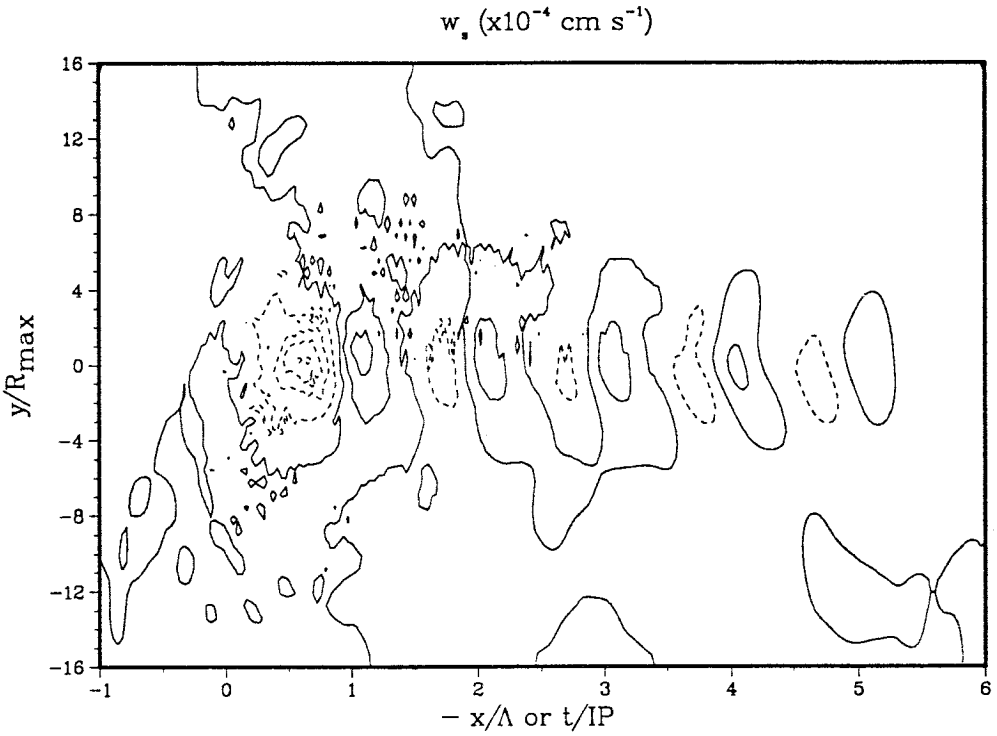

FIG. 8. Contours of the vertical velocity field at 5 m derived by vertically integrating the horizontal divergence term from the 17-level model contoured at intervals of 2×10^{-4} cm s^{-1}. The axes are scaled as in Fig. 5.

the addition of more modes in the least square fits. That is, adding more baroclinic modes to the analysis does not remove energy from the previous modal amplitudes, thereby reducing residual variance between the model and modal profiles.

In the wake of the hurricane ($x \approx 2\Lambda$), demodulated horizontal velocity profiles indicate that the barotropic mode contributes about 5–6 cm s^{-1} (Fig. 11). This current is relatively weak compared to the amplitude of the first baroclinic mode in the mixed layer of about 35 cm s^{-1}. Adding these two modes in the mixed layer reduces the residual current (model modal profile) to about 4–5 cm s^{-1}. The second baroclinic mode is 180° out of phase with the barotropic and first baroclinic modes, suggesting minimal influence on mixed layer currents compared to the model profile. However, this mode plays an important role at the mixed layer base and upper part of the thermocline in that it follows the slope of the model profile. In the bottom layers (i.e., 400 m), the first and second baroclinic modes sum to a value of about 20–22 cm s^{-1} compared to a model profile of 14–16 cm s^{-1}. Thus, adding the positive barotropic current of 5–6 cm s^{-1} reduces the amplitude differences to about 2 cm s^{-1}. The third baroclinic mode does not significantly contribute to the model profile but has a relative maximum of 2 to 4 cm s^{-1} in the high-shear zone between the mixed layer and thermocline. Higher-order baroclinic modes contribute significantly to the vertical shear and mixing events across this zone during the passage of strong atmospheric forcing events (Niiler and Kraus 1977).

c. Horizontal velocity

The horizontal distribution of the barotropic and first baroclinic modes indicates a concentration of modal energies between $y = 1$ to $3\,R_{max}$ (Fig. 12). The barotropic component has a maximum amplitude of about 7 cm s^{-1} near $y = 2R_{max}$, having a range of 4–7 cm s^{-1} over five IPs in accord with the velocity structure (Fig. 7). SCE originally found a value of about 10–11 cm s^{-1} in the demodulated signals due to the manner in which the real parts of the demodulated velocities were combined prior to the modal fits. The first baroclinic mode amplitude dominates the response with relative maxima of 55–58 cm s^{-1}. In the mixed layer these two modes are in phase, whereas in the lower layers they are out of phase, as indicated by the vertical structure equation shown in Figs. 2 and 11.

The ratio of the amplitudes of the barotropic mode (7 cm s^{-1}) and first baroclinic mode (58 cm s^{-1}) is about 0.13. The first baroclinic mode dominates the near-inertial wave band, accounting for about 60% of the current amplitude compared to about 7% for the barotropic component for a mixed layer inertial current of 90–100 cm s^{-1}. The barotropic contribution is

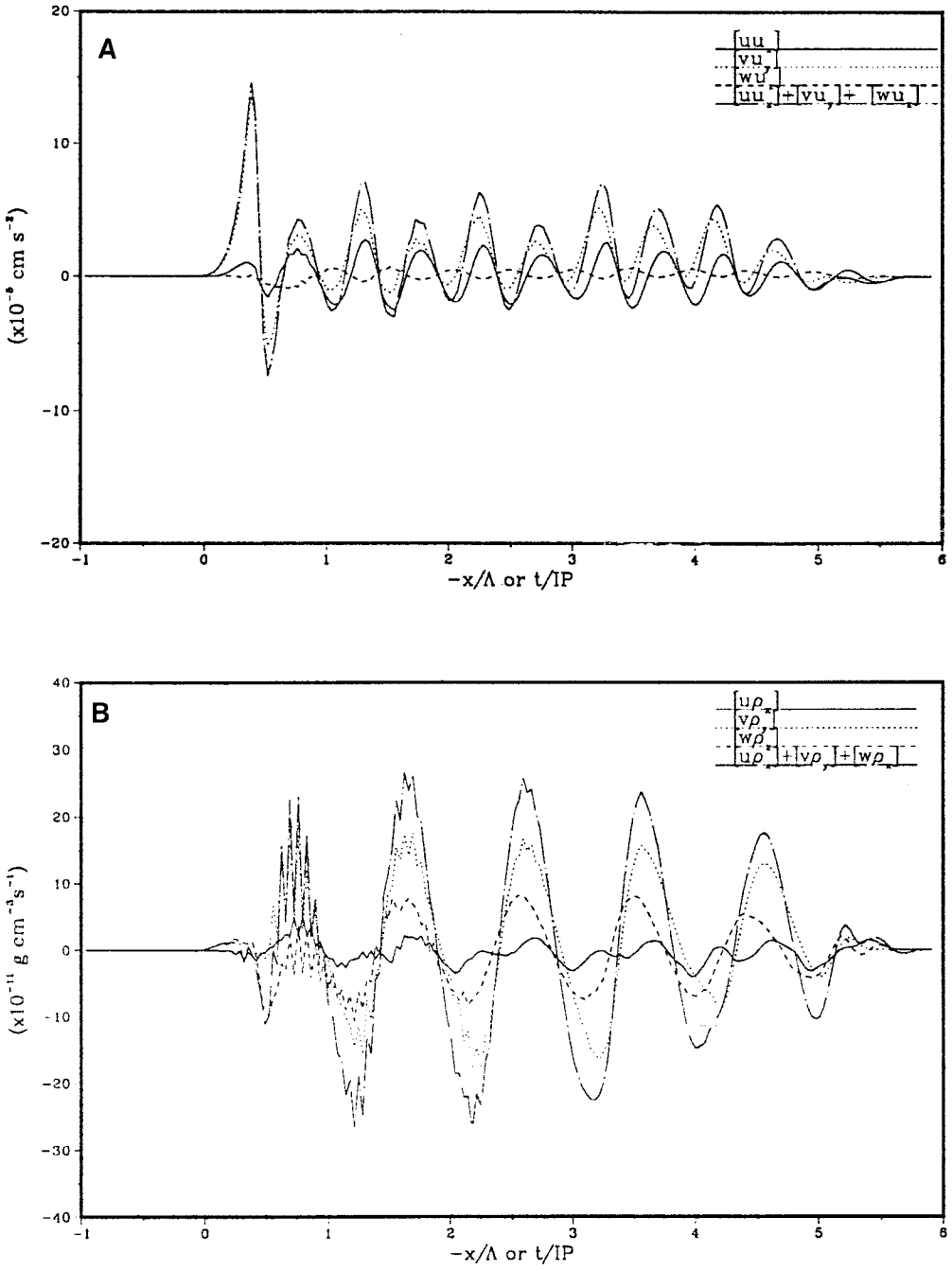

FIG. 9. Nonlinear contributions from the depth-averaged (a) alongtrack momentum terms ($\times 10^{-5}$ cm s^{-2}) for $[uu_x]$ (solid), $[v_y]$ (dotted), $[wu_z]$ (dashed); and $[uu_x] + [vu_y] + [wu_z]$ (chain-dashed), and (b) density terms ($\times 10^{-11}$ g cm^{-3} s^{-1}) for $[u\rho_x]$ (solid), $[v\rho_y]$ (dotted), $[w\rho_z]$ (dashed), and $[u\rho_x] + [v\rho_y] + [w\rho_z]$ (chain-dashed) in the alongtrack direction at y = $0R_{max}$.

close to the estimates predicted by Rossby (1938) and about 2% more than that estimated by Veronis (1956). The ratio of the barotropic to the first baroclinic modal energy is about 0.02 (2%), and a large fraction of the vertical structure variability can be described by linear dynamics.

d. Vertical velocity

The vertical velocities, determined by vertically integrating the horizontal divergence field from the bottom at $z = -D$ to 5 m, and the vertical velocity at the sea surface (η_t) are combined to form 18-level profiles and

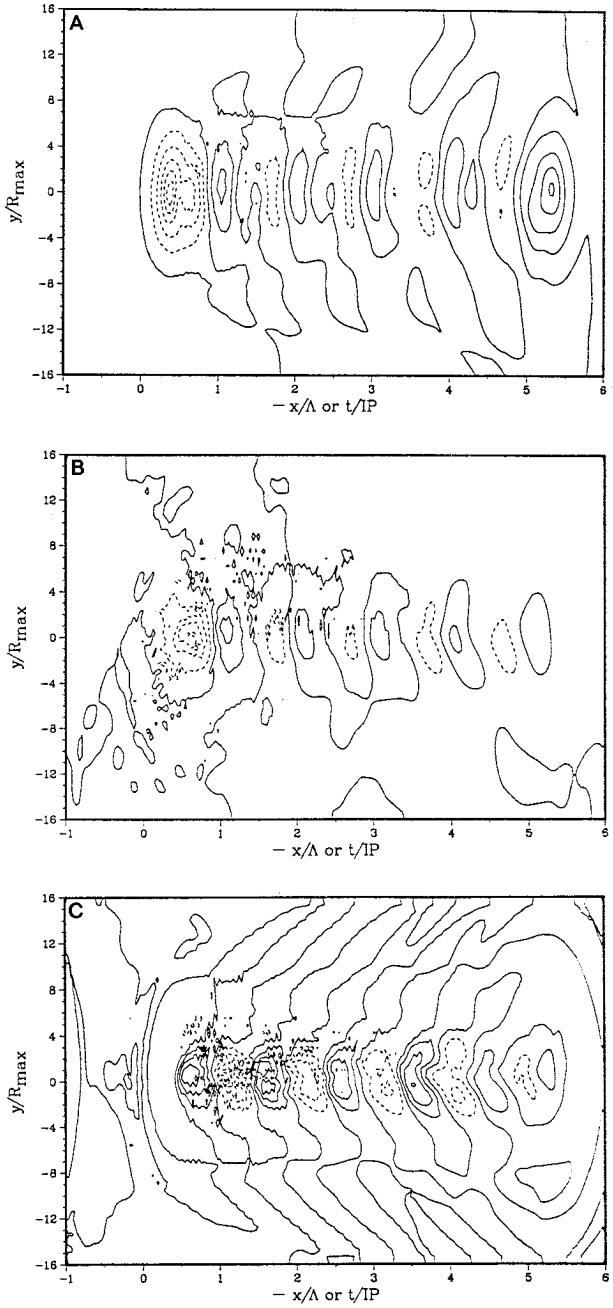

FIG. 10. Contours of (a) $\eta_t(\times 10^{-4}$ cm s$^{-1})$, (b) $-D\partial[u]/\partial x - D\partial[v]/\partial y(\times 10^{-4}$ cm s$^{-1})$, and (c) $-\partial\eta u_s/\partial x - \partial\eta v_s/\partial y$ $(\times 10^{-5}$ cm s$^{-1})$ from the 17-level model contoured at intervals of 2×10^{-4} cm s^{-1} for panels (a) and (b) and 1×10^{-5} cm s^{-1} in panel (c). The axes are scaled as in Fig. 5.

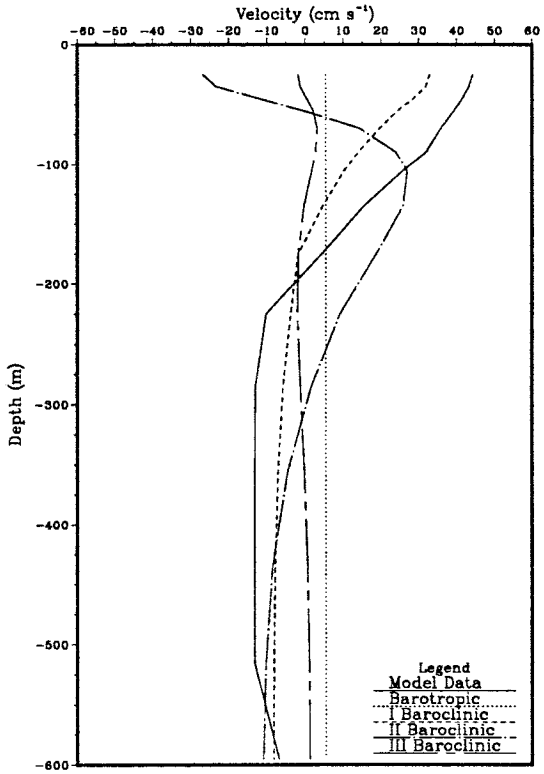

FIG. 11. Vertical profile of the demodulated current (cm s^{-1}) (solid) decomposed into the barotropic mode (dotted), first baroclinic mode (dashed), second baroclinic mode (chain-dotted), and third baroclinic mode (chain-dashed) in the model domain.

are fit to the barotropic mode and first baroclinic mode eigenfunctions (Fig. 2). The maximum vertical velocity for the barotropic mode current (product of the modal amplitudes and corresponding eigenfunction) at the sea surface is about 2×10^{-3} cm s^{-1}, whereas the corresponding value for the first baroclinic mode current is 4×10^{-5} cm s^{-1} (Fig. 13). There are marked similarities between the barotropic modal component here and that determined from the sea surface variations (Fig. 10a). In addition to dominating surface processes by a factor of about 50, the barotropic vertical velocity is oscillatory, which agrees with the nonlinear interaction terms for depth-averaged mass divergence (Fig. 9b). The vertical velocity of the first baroclinic mode is directly out of phase with the barotropic component. The predominance of the first mode is expected because it has a maximum in the thermocline that presumably balances pressure perturbations due to surface oscillations. In continuously stratified flows, upwelling and downwelling signatures are distributed throughout the water column, which is consistent with the velocity and temperature observations in Fig. 1. The coupling of the barotropic and first baroclinic modes described above implies that weak barotropic and strong baroclinic phenomena are associated with the evolving wake of a hurricane.

e. Surface displacements

The modal vertical velocities at the surface are integrated in time ($\Delta x = -U_h \Delta t$) to estimate surface height variations (Fig. 14). Given the vertical velocities associated with the barotropic mode at the surface, the corresponding heights oscillate $\pm$ 4 cm. These displace-

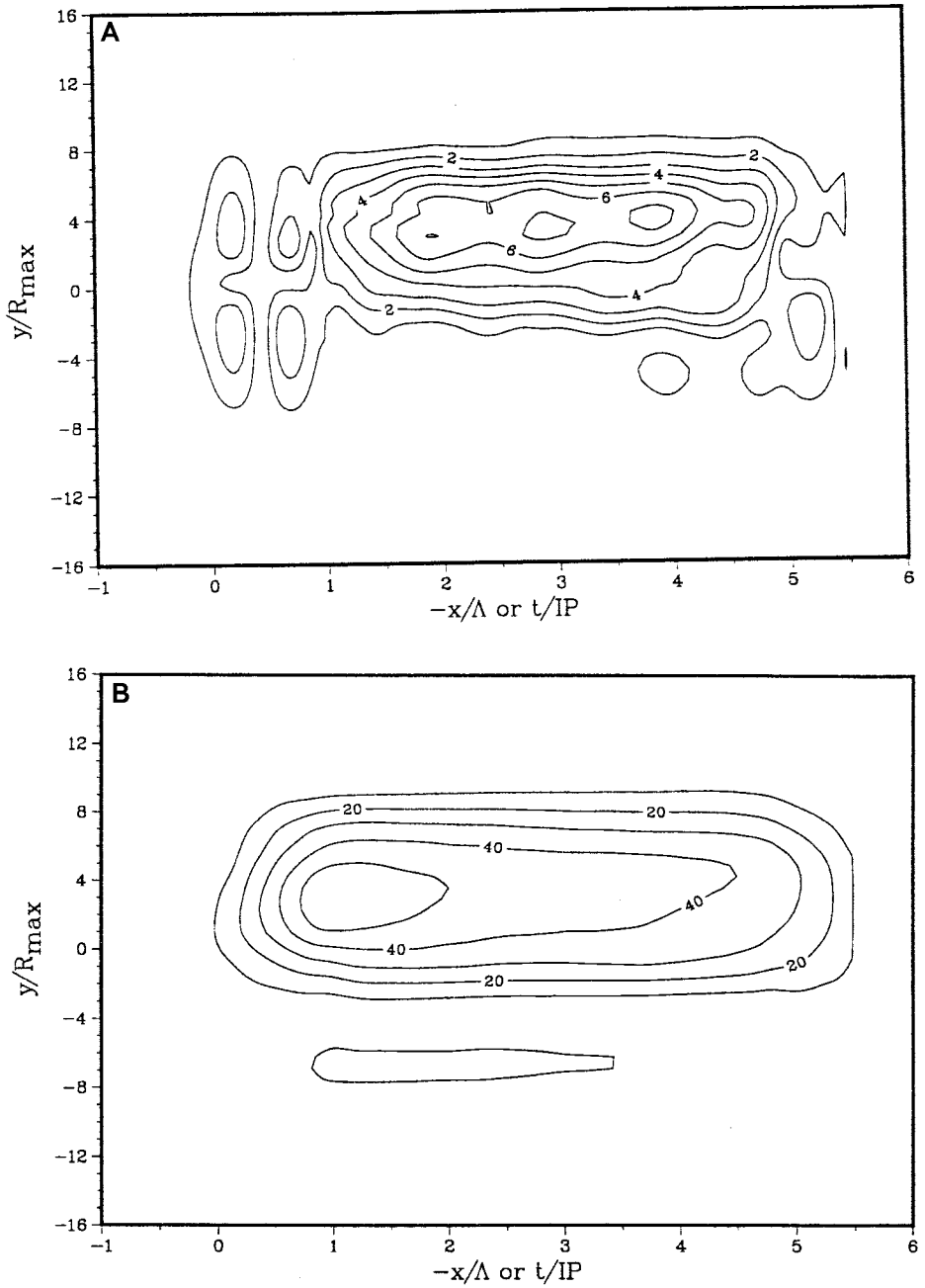

FIG. 12. Modal amplitudes (cm s^{-1}) of the (a) barotropic mode and (b) first baroclinic mode estimated from the real part of the demodulated horizontal velocity amplitudes at 1.03*f* fit to the horizontal velocity eigenmodes from Fig. 2, based on singular value decomposition as Fig. 11. The axes are scaled in terms of Fig. 5 and the contour intervals are 1 and 10 cm s^{-1} for modes 0 and 1, respectively.

ments agree with the cells isolated in Fig. 7 (after removal of the steady-state signals), indicating that a large fraction of the sea surface undulations in the multilevel simulations are associated with the barotropic mode. The first baroclinic mode contributes about 0.2–0.4 cm to these surface oscillations and are 180° out of phase with the barotropic mode surface elevation field. Similar results for the baroclinic mode effects on the free surface are found by integrating the vertical velocities from a forced linear model (Shay et al. 1989).

The contributions of the barotropic mode and first baroclinic mode are directly compared to the sea surface undulations isolated by removing the steady-state part of the surface depression (Fig. 15). Apart from the initial spinup at $x = 0.5\ \Lambda$, the barotropic oscillations of about ± 4 cm are nearly in phase with the sea surface vari-

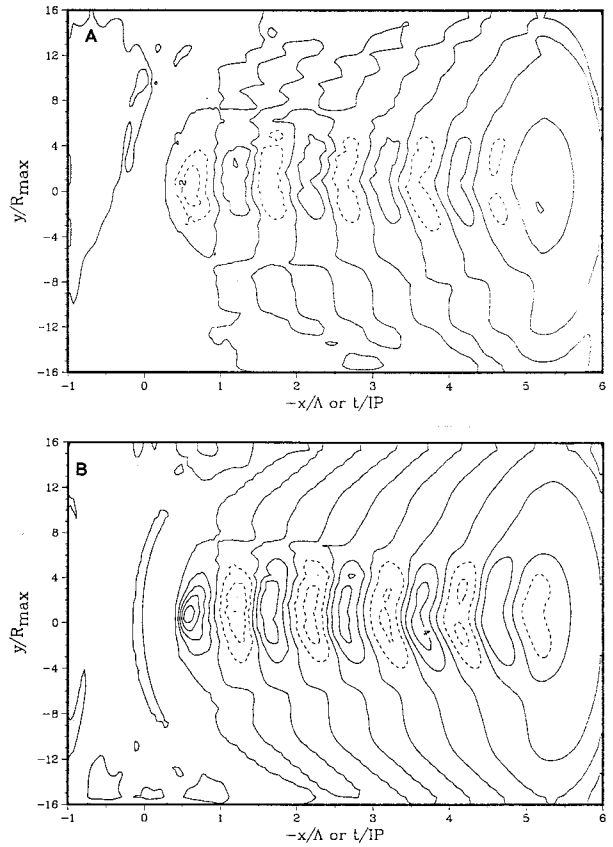

FIG. 13. Surface vertical velocities of the (a) barotropic mode ($\times 10^{-3}$ cm s^{-1}) and (b) first baroclinic mode ($\times 10^{-5}$ cm s^{-1}) estimated from the 18 levels (including the surface η_i) based on a fit of the vertical velocities to the eigenfunctions from Fig. 2 using singular value decomposition as in Fig. 11, and multipling by the free surface value for each mode. The axes are scaled as in Fig. 5 and the contour intervals are at 1 and 0.1 cm s^{-1}, for panels (a) and (b), respectively.

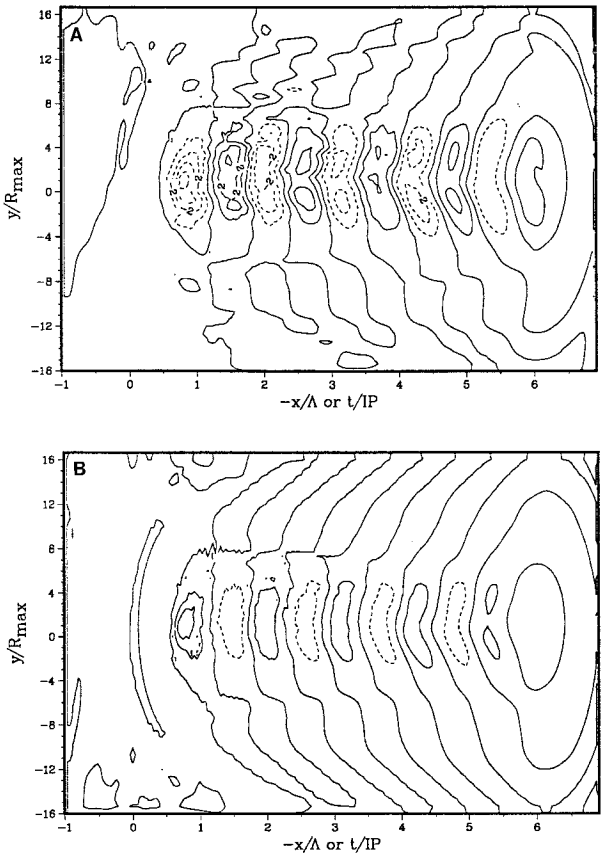

FIG. 14. Surface deflections associated with the (a) barotropic mode (cm) and (b) first baroclinic mode ($\times 10^{-1}$ cm) estimated by integrating Fig. 13 with respect to time or alongtrack distance. Notice that the surface deflections are a factor of 40 smaller for the baroclinic terms compared to the barotropic mode counterpart. The axes are scaled in terms of Fig. 5; and the contour intervals are 1 and 0.1 cm intervals for (a) and (b), respectively.

ability starting at $x = 1.5\Lambda$. While the barotropic displacements lead the surface undulations by $x \approx 0.1\Lambda$, the two signals show marked consistency. The first baroclinic mode amplitudes range from ± 0.2 to 0.4 cm and are slightly out of phase with the more energetic barotropic counterpart at the surface. This baroclinic effect, which is considerably less than those predicted in analytical studies (Ginis and Sutyrin 1995), represents a secondary peak in the sea surface oscillations induced by nonlinear interaction terms in the momentum equations (Fig. 9a). Since the first mode has larger surface values than the other baroclinic modes, their relative contributions decrease with increasing mode number. Thus, the surface height signals (90%–95%) appear to behave linearly after excitation by the nonlinear interactions associated with the depth-averaged mass divergence field.

5. Conclusions

The results found in SCE have been revisited to examine if there is an oscillatory barotropic current in the near-inertial wave band due to the replacement of a rigid lid with a free surface in a 17-level primitive equation model, to determine the forcing mechanism, and to assess whether the resulting currents are linear, nonlinear, or weakly nonlinear. The barotropic response not only includes a sea surface depression with a cyclonically rotating current field in geostrophic balance, but also weak barotropic current oscillations. While there is no difference between the geostrophic current and the depth-averaged flow in a one-layer model, the net difference of 7–8 cm s^{-1} between the same signals in the multilevel model is due to the existence of a near-inertially rotating current. This current rotates in the opposite direction to the flow around the steady-state depression and is directed into the pressure gradient (Pedlosky 1979). This barotropic Poincaré wave mode is part of the vertical structure of near-inertial motions in a stratified fluid subjected to a free surface boundary condition. Since there are no horizontal density gradients (or depth-averaged mass divergence) in the one-layer

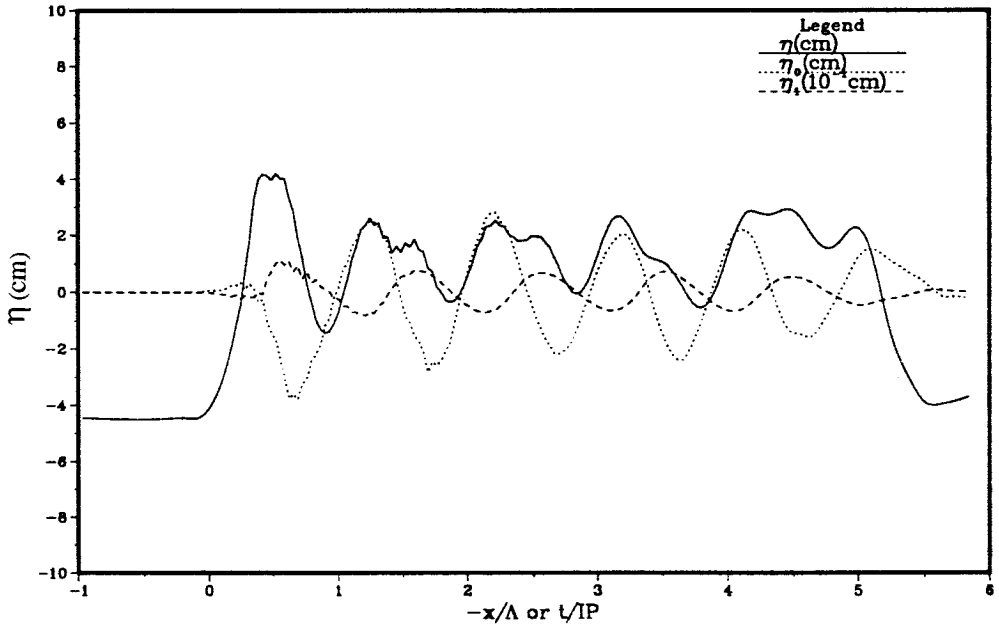

FIG. 15. Surface deflections (solid) in the alongtrack direction in cm simulated by the 17-level model (see Fig. 5) and the corresponding contributions from the barotropic (dotted) corresponding to Fig. 14a, and first baroclinic (dashed) corresponding to Fig. 14b modes at y = 0. Notice that the barotropic mode dominates the balance since the first baroclinic mode contribution is mm.

model, there is an absence of free surface oscillations and a barotropic near-inertial current.

Free surface undulations and the associated vertical velocities are driven by the depth-averaged nonlinear interaction terms $[v\rho_y]$ and $[w\rho_z]$ or the depth-averaged mass divergence in the multilevel primitive equation model. Divergence terms of 8×10^{-4} s^{-1} balance the time-dependent surface deflections, while the surface transport terms contribute less than 10% to free surface displacements. The surface deflections represent an interaction between the baroclinic and barotropic terms in the depth-averaged mass divergence (Chang 1985) and are not a pure barotropic response (SCE). The dispersion of Rossby waves will also play a role in the relaxation of the sea surface depression (Geisler 1970). However, the oscillatory motion described here is on an *f* plane, and is required for the dispersion of the surface depression (Rossby 1938), even though scale analysis suggests that to $O(10\%)$ the divergence terms can be neglected.

The fit of the eigenfunctions to the demodulated currents indicates a depth-independent velocity of about 7–8 cm s^{-1} and agrees with that found by removing the geostrophic component from the depth-averaged flow. In SCE, this simulated component was found to be about 10–11 cm s^{-1}, equating to an overestimation of about 3 cm s^{-1}. In an ocean 465 m deep for CMA3 (i.e., Fig. 1), the equivalent value is 9–10 cm s^{-1}, which agrees well with the observed depth-averaged current. The first baroclinic mode dominates the current response having a maximum amplitude of 58 cm s^{-1} compared to the 7 cm s^{-1} barotropic flow (yielding an energy of about 2% of that of the first mode).

The phase relation between the first baroclinic and barotropic modes produces an upward vertical velocity in the thermocline and downward vertical velocity at the sea surface, respectively. The modal fit of the vertical velocities including the surface value (η_t) reveals a barotropic vertical velocity that is nearly 50 times larger (2×10^{-3} cm s^{-1}) than the first baroclinic mode contribution (4×10^{-5} cm s^{-1}) at the sea surface. Since the first-mode baroclinic eigenfunction at the sea surface is in phase with the thermocline displacement, upwelling in the thermocline coincides with upward motion at the free surface. However, surface deflections of ± 4 cm are associated with the barotropic mode compared to 0.2–0.4 cm for the first baroclinic mode, and they progressively decrease for higher modes. Since the free surface is minimally affected by the baroclinic modes, this result underscores the rationale behind the rigid-lid approximation in simulating the ocean's baroclinic response imposed in numerical models.

The three-dimensional velocities exhibit marked linear behavior, suggesting that the zeroth-order state of the ocean response may be characterized as either predominately linear or perhaps weakly nonlinear. Given the consistencies in the interpretation of the observed and simulated velocity signals from the analytical and numerical models within the context of linear near-inertial wave dynamics, an alternative viewpoint has been suggested here that differs with numerical (Cooper and Thompson 1989) and theoretical (Ginis and Sutyrin

1995) studies. This contrasting perspective is motivated by observations in Hurricanes Allen (Brooks 1983) and Frederic (Shay and Elsberry 1987) in the Gulf of Mexico, Typhoons Ian and Victor over the Australian continental shelf (Hearn and Holloway 1990), and numerical studies (Chang 1985; Signorini et al. 1992) supporting the premise that the ocean response contains weak barotropic and strong baroclinic near-inertial oscillations. This view is also consistent with the original findings by Rossby (1938) and Cahn (1945). In the absence of this barotropic component, the sea surface depression remains indefinitely, creating an imbalance in the height and velocity fields, a geophysically unrealistic situation.

Acknowledgments. Tak Fung at the Naval Research Laboratory collapsed the 17-level model into a one-layer model and provided the simulated fields. The authors thank Richard Garvine and Xin Liu for their comments and Isaac Ginis and George Sutyrin for focusing attention on the free surface. We thank Claes Rooth, Russell Elsberry, and Richard Greatbatch for sharing their insights regarding the theme of this manuscript. S. Daniel Jacob provided valuable programming support. The first author gratefully acknowledges support from the Office of Naval Research (N00014-93-1-0417).

REFERENCES

Brooks, D., 1983: The wake of Hurricane Allen in the western Gulf of Mexico. *J. Phys. Oceanogr.,* **13,** 117–129.

Cahn, A., 1945: An investigation of free oscillations of a simple current system. *J. Meteor.,* **2,** 113–119.

Chang, S. W., 1985: Deep ocean response to hurricanes revealed by an ocean model with a free surface. *J. Phys. Oceanogr.,* **15,** 1847–1858.

Cooper, C., and J. D. Thompson, 1989: Hurricane generated currents on the outer continental shelf. Part 1: Model formulation and verification. *J. Geophys. Res.,* **94,** 12 513–12 540.

Geisler, J. E., 1970: Linear theory on the response of a two layer ocean to moving hurricane. *Geophys. Fluid Dyn.,* **1,** 249–272.

Gill, A. E., 1984: On the behavior of internal waves in the wakes of storms. *J. Phys. Oceanogr.,* **14,** 1129–1151.

Ginis, I., and G. Sutyrin, 1995: Analytical and numerical studies of the hurricane-generated depth-averaged currents and sea surface effects. *J. Phys. Oceanogr.,* **25,** 1218–1242.

Greatbatch, R. J., 1983: On the response of the ocean to a moving storm: The nonlinear dynamics. *J. Phys. Oceanogr.,* **13,** 357–367.

Hearn, C. J., and P. E. Holloway, 1990: A three-dimensional barotropic model of the response of the Australian North West Shelf to tropical cyclones. *J. Phys. Oceanogr.,* **20,** 60–80.

Hopkins, C., 1982: Ocean response to hurricane forcing. M.S. thesis, Department of Meteorology, Naval Postgraduate School, 89 pp.

Lai, D. Y., and T. B. Sanford, 1986: Observations of hurricane-generated, near-inertial slope modes. *J. Phys. Oceanogr.,* **16,** 657–666.

Leblond, P. H., and L. A. Mysak, 1979: *Waves in the Ocean.* Elsevier Oceanography Series, Vol. 20, Elsevier, 602 pp.

Mayer, D., H. O. Mofgeld, and K. D. Leaman, 1981: Near-inertial internal waves on the outer shelf of the middle Atlantic Bight in the wake of Hurricane Belle. *J. Phys. Oceanogr.,* **11,** 86–106.

Niiler, P. P., and E. B. Kraus, 1977: One-dimensional models of the upper ocean. *Modelling and Prediction of the Upper Layers of the Ocean,* E. B. Kraus, Ed., Pergamon Press, 143 pp.

Pedlosky, J., 1979: *Geophysical Fluid Dynamics.* Springer-Verlag, 625 pp.

Powell, M. D., 1982: The transition of the Hurricane Frederic boundary layer wind field from the open Gulf of Mexico to landfall. *Mon. Wea. Rev.,* **110,** 1912–1932.

Press, W. H., S. A. Teukoulsky, B. P. Flannery, and W. T Vetterling, 1989: *Numerical Recipes.* Cambridge University Press, 702 pp.

Price, J. F., 1983: Internal wave wake of a moving storm. Part I: Scales, energy budget and observations. *J. Phys. Oceanogr.,* **13,** 949–965.

Rossby, C. G., 1938: On the mutual adjustment of pressure and velocity distributions in certain simple current systems. *J. Mar. Res.,* **1,** 239–263.

Shay, L. K., and R. L. Elsberry, 1987: Near-inertial ocean current response to Hurricane Frederic. *J. Phys. Oceanogr.,* **17,** 1249–1269.

——, ——, and P. G. Black, 1989: Vertical structure of the ocean current response to a hurricane. *J. Phys. Oceanogr.,* **19,** 649–669.

——, S. W. Chang, and R. L. Elsberry, 1990: Free surface effects on the near-inertial current response to a hurricane. *J. Phys. Oceanogr.,* **20,** 1405–1424.

Signorini, S. R., J. S. Wei, and C. D. Miller, 1992: Hurricane-induced surge and currents on the Texas and Louisiana shelf. *J. Geophys. Res.,* **97,** 2229–2242.

Starr, R. B., and G. A. Maul, 1982: Physical oceanographic observations in the eastern Gulf of Mexico 1979–1980 for a potential OTEC Site. NOAA Tech. Memo. ERL-AOML-50, Atlantic Oceanographic and Meteorological Laboratories, Miami, FL, 205 pp.

Veronis, G. 1956: Parition of energy between geostrophic and non-geostrophic oceanic motions. *Deep-Sea. Res,* **3,** 157–177.